Detection of electromagnetic pulses produced by hypervelocity micro particle impact plasmas

Sigrid Close, Ivan Linscott, Nicolas Lee, Theresa Johnson, David Strauss, Ashish Goel, Alexander Fletcher, David Lauben, Ralf Srama, Anna Mocker, and Sebastian Bugiel

Citation: Physics of Plasmas (1994-present) **20**, 092102 (2013); doi: 10.1063/1.4819777
View online: http://dx.doi.org/10.1063/1.4819777
View Table of Contents: http://scitation.aip.org/content/aip/journal/pop/20/9?ver=pdfcov
Published by the AIP Publishing

Detection of electromagnetic pulses produced by hypervelocity micro particle impact plasmas

Sigrid Close,[1] Ivan Linscott,[2] Nicolas Lee,[1] Theresa Johnson,[1] David Strauss,[2] Ashish Goel,[1] Alexander Fletcher,[1] David Lauben,[2] Ralf Srama,[3] Anna Mocker,[3] and Sebastian Bugiel[3]
[1]*Department of Aeronautics and Astronautics, Stanford University, Stanford, California 94305, USA*
[2]*Department of Electrical Engineering, Stanford University, Stanford, California 94305, USA*
[3]*Institut für Raumfahrtsysteme, Universität Stuttgart, Pfaffenwaldring 29, 70569 Stuttgart, Germany*

(Received 3 April 2013; accepted 6 August 2013; published online 3 September 2013)

Hypervelocity micro particles (mass < 1 ng), including meteoroids and space debris, routinely impact spacecraft and produce plasmas that are initially dense ($\sim 10^{28}$ m^{-3}), but rapidly expand into the surrounding vacuum. We report the detection of radio frequency (RF) emission associated with electromagnetic pulses (EMPs) from hypervelocity impacts of micro particles in ground-based experiments using micro particles that are 15 orders of magnitude less massive than previously observed. The EMP production is a stochastic process that is influenced by plasma turbulence such that the EMP detection rate that is strongly dependent on impact speed and on the electrical charge conditions at the impact surface. In particular, impacts of the fastest micro particles occurring under spacecraft charging conditions representative of high geomagnetic activity are the most likely to produce RF emission. This new phenomenon may provide a source for unexplained RF measurements on spacecraft charged to high potentials. © *2013 AIP Publishing LLC*.
[http://dx.doi.org/10.1063/1.4819777]

I. INTRODUCTION

Large (mass $> 10^{-3}$ g) hypervelocity objects, including meteoroids and space debris, are known to cause mechanical damage upon impact with a spacecraft. However, due to the mass flux, spacecraft are much more likely to be impacted by small (<1 μg) particles that travel with speeds of approximately 11 to 72 km/s.[1–3] Furthermore, the probability of failure is much higher during impacts by fast particles due to the strong dependence between charge production and speed, yet the resulting electrical effects remain unknown. Previous efforts have found a temporal link between electrical anomalies and meteoroid shower activity, including anomalies on Olympus,[4] Landsat-5, ALOS, and ADEOS-II.[5] However, attributing meteoroid impact as the cause of the electrical anomaly remains weak due to a lack of on-orbit diagnostics. Furthermore, recent research has shown that the background sporadic population is actually dominant over shower particles at sizes <1 μg, suggesting that any attempt to correlate shower activity to on-orbit anomalies is remarkably incomplete due to the much greater probability of impact by these small particles.[6–9] It is possible that many of the electrical anomalies that cannot be temporally associated with solar activity may in fact be associated with impacts by small, fast particles.

Radio frequency (RF) signals have been associated with hypervelocity particle impacts both in space and in laboratory studies. Space experiments include the Voyager planetary radio astronomy experiment as well as more recent measurements by Cassini and the STEREO spacecraft. Meyer-Vernet *et al.*[10,11] detected nanoparticles impacts on STEREO's S/WAVES instrument, while St. Cyr *et al.*[12] correlated micron-sized dust impacts detected by S/WAVES with the white light instrument on the SECCHI suite. Gurnett *et al.*[13] and Wang *et al.*[14] used the Cassini Radio and Plasma Wave Science (RPWS) to detect RF signals during impacts by dust particles near Saturn's ring plane. Warwick *et al.*[15,16] and Aubier *et al.*[17] also detected radio noise during Voyager 1 and 2 ring plane crossings at Saturn using the Planetary Radio Astronomy (RPA) instruments. Ground-based experiments showing RF detection have been limited to large hypervelocity particle impacts. Crawford and Shultz[18,19] used the two-stage hydrogen light gas gun at the NASA Ames Vertical Gun Range to shoot 0.16–0.37 g aluminum spheres into powered dolomite targets at speeds ranging from 5 to 7 km/s. Magnetic search coils were used to detect magnetic fields generated by impact plasmas and charge detection plates were used to measure electric current as a function of angle and time. Microwave emission has been measured in experiments at the Institute of Space and Astronautical Science in Japan using both light gas gun and rail gun facilities.[20–23] Bianchi *et al.*[24] observed RF signals from impacts of $\sim$1 g aluminum projectiles on rocks. Martelli and Cerroni,[25] as well as O'Keefe and Thiel[26] in 1995 modeled electromagnetic radiation from fracture of rock and other brittle materials. Foschini[27] in 1998 modeled radiation of electromagnetic energy from plasma clouds formed by hypervelocity impacts of meteoroids. However, to date, RF emission from small (mass $< 10^{-3}$ g) micro particle impacts has not been detected in the laboratory.

Upon impact, micro particles produce a gas-plasma plume that is composed of fragmented, vaporized, and ionized target and projectile material.[28] For projectiles exceeding the target material sound speed, the initial plasma density increases strongly with impact speed (and weakly with particle mass), becoming comparable to that of the

parent solid-phase material; the initial Debye length is much smaller than the size of the plume.[29] Laboratory measurements characterizing impact plasma generation[30–32] and crater size[33,34] indicate that charge production follows a power law ranging from $mv^{2.8}$ to $mv^{4.7}$, where m is particle mass and v is impact speed. The plasma expands in a collisionless (i.e., vacuum) environment over nanoseconds, decreasing the plasma density with a corresponding increase in the Debye length. Within tens of nanoseconds, the Debye length exceeds the size of the plasma plume, rendering the plume transparent to external electric fields. If these external fields are small, the plasma can continue to expand freely, exhibiting localized oscillations and instabilities that can produce RF emission in the form of an electromagnetic pulse (EMP); the plasma maintains general charge quasineutrality as it dissipates. If a large external field exists, the positive ions and electrons will be swept in opposite directions, creating a sudden, bulk acceleration of charge that can also produce RF emission in the form of an EMP. The EMP, which is a broadband electromagnetic burst of energy, can be distorted by turbulence in the plasma, which produced density irregularities that create regions of weaker and stronger Debye shielding and leads to corresponding asymmetries in the radiated field. This model of plasma generation and expansion, which is strongly dependent on impact speed, is valid for even the smallest hypervelocity particles.

II. GROUND-BASED IMPACT EXPERIMENT

We conducted a series of experiments in 2011 using a Van de Graaff dust accelerator at the Max Planck Institute (MPI) for Nuclear Physics that allowed for vacuum conditions and particle speeds representative of impacts on spacecraft. We had previously conducted an experimental campaign at the facility in 2010 to characterize the expansion speed of impact plasmas.[35] Electrostatic dust accelerators including the MPI Van de Graaff dust accelerator use a high-voltage device to accelerate charged micro particles. The micro particles must therefore be conductive, and the size of the micro particle is intrinsically linked to the speed because of the dependence on the surface charge to mass ratio. Electrostatic accelerators are the only technology capable of accelerating micro particles to speeds representative of the fastest meteoroids, which typically impact spacecraft at speeds between 20 and 60 km/s.[36] Additionally, the lack of a working fluid in the acceleration mechanism ensures a clean ambient environment compared to light gas guns, plasma drag accelerators, and other ground-based hypervelocity impact facilities. Mocker *et al.*[37] provide a comprehensive description of the accelerator technology.

The experimental conditions we obtained include (a) representative micro particle speeds of 3 to 66 km/s, (b) a pressure within the 1.4 m test chamber maintained between 2.5×10^{-4} Pa and 1.0×10^{-3} Pa, which allows for vacuum conditions that permit collisionless free expansion of the impact plasma, and (c) micro particle sizes, with masses between 10^{-16} and 10^{-11} g, that were composed of iron and impacted, but did not penetrate, a target in the impact chamber. These masses, however, are approximately 9 orders of magnitude smaller than what is commonly encountered in orbit. Due to the nature of the accelerator, the mass and velocity of the micro particles were coupled, such that the highest mass particles corresponded to the slowest velocities.

The chamber was instrumented with sensors including (a) a photomultiplier tube (PMT) to record the optical flash that occurs upon impact, (b) plasma sensors, including two retarding potential analyzers (RPAs) or Faraday Plate Arrays (FPAs) to characterize the net current associated with the expanding plasma, and (c) six patch antennas tuned to 315 MHz and 916 MHz to measure RF emission that were specifically designed to detect electromagnetic (not electrostatic) emission, as discussed in Sec. V. Although current technology limits our ability to detect RF at these wavelengths in the far-field in any ground-based hypervelocity chamber, there is no impediment to performing a measurement in the near-field that can produce meaningful understanding of the electromagnetic field in the vicinity of the source. Figure 1 shows the geometric configuration of the chamber with the targets and sensors. The PMT was a Hamamatsu model H10721-110, and the patch antennas were embedded quarter-wave chip antennas surface-mounted individually on PCBs with low noise amplifiers (LNAs). The other sensors were custom-built. The targets, shown in Fig. 2, included passive (un-instrumented) materials, including tungsten, aluminum, and representative spacecraft components donated by Likar of Lockheed Martin, as well as a target with an active electric field (E-field) sensor, which was biased to a range of potentials from 0 to ±1000 V to represent spacecraft charging conditions.[38] We positioned an additional E-field sensor similar in construction but oriented to the side and perpendicular to the target (E-field

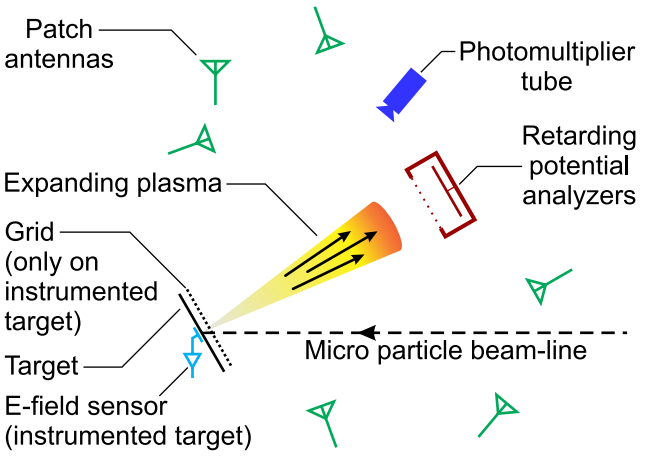

FIG. 1. Side view of the test chamber with sensors and targets. The accelerator fires micro particles from right to left. The six patch antennas were spatially distributed throughout the chamber. The targets were oriented +30° upward from the incident micro particle beam-line. A biasing grid on the tungsten target with the E-field sensor was suspended 1 mm over the impact surface and was coupled to the biasing potential. The RPAs were positioned 85 and 65 mm in range at ±30° azimuth and 30° elevation from the impact point, subtending solid angles of 0.29 and 0.18 steradian, respectively. The PMT was at 110 mm range and 50° elevation from impact point (20° relative to the target normal). The patch antennas were at 12 to 22 cm range, spanning the outward-facing hemisphere relative to the target surface. The E-field side was positioned 12 mm from the beamline oriented 90° relative to the target surface and in the vertical plane.

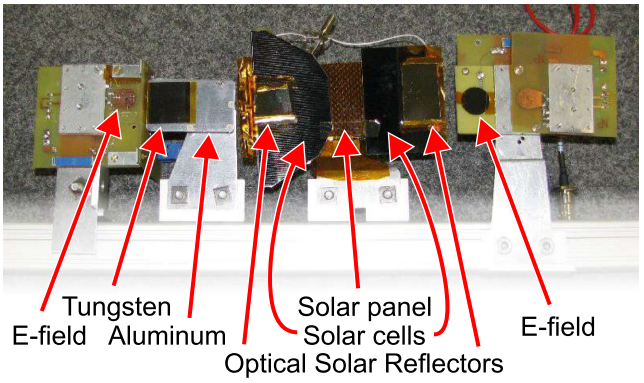

FIG. 2. Targets used in the experimental campaign. These targets were mounted on a common frame, which could be translated horizontally within the chamber to move each target individually into the projectile beam line. Reprinted with permission from Lee *et al.*, Phys. Plasmas **20**, 032901 (2013). Copyright 2013 American Institute of Physics.

side). The E-field sensors, which are conceptually stub antennas connected to a low-noise amplifier, provided a measurement of RF signal, independent of the patch antennas, allowing an estimate of electric charge production and displacement current. The targets were thick enough to appear semi-infinite to the impacting micro particle; tungsten was chosen because it is known to produce substantial charge upon hypervelocity impact.[39,40]

III. SENSOR MEASUREMENTS

An example of the measurements obtained from the sensor suite in the impact chamber is presented in Fig. 3. These data were generated by an iron micro particle with a mass of 1.4×10^{-15} g impacting a tungsten foil at 40 km/s; the foil was under a grid biased to +1000 V, which is equivalent to biasing the actual target to −1000 V and is representative of

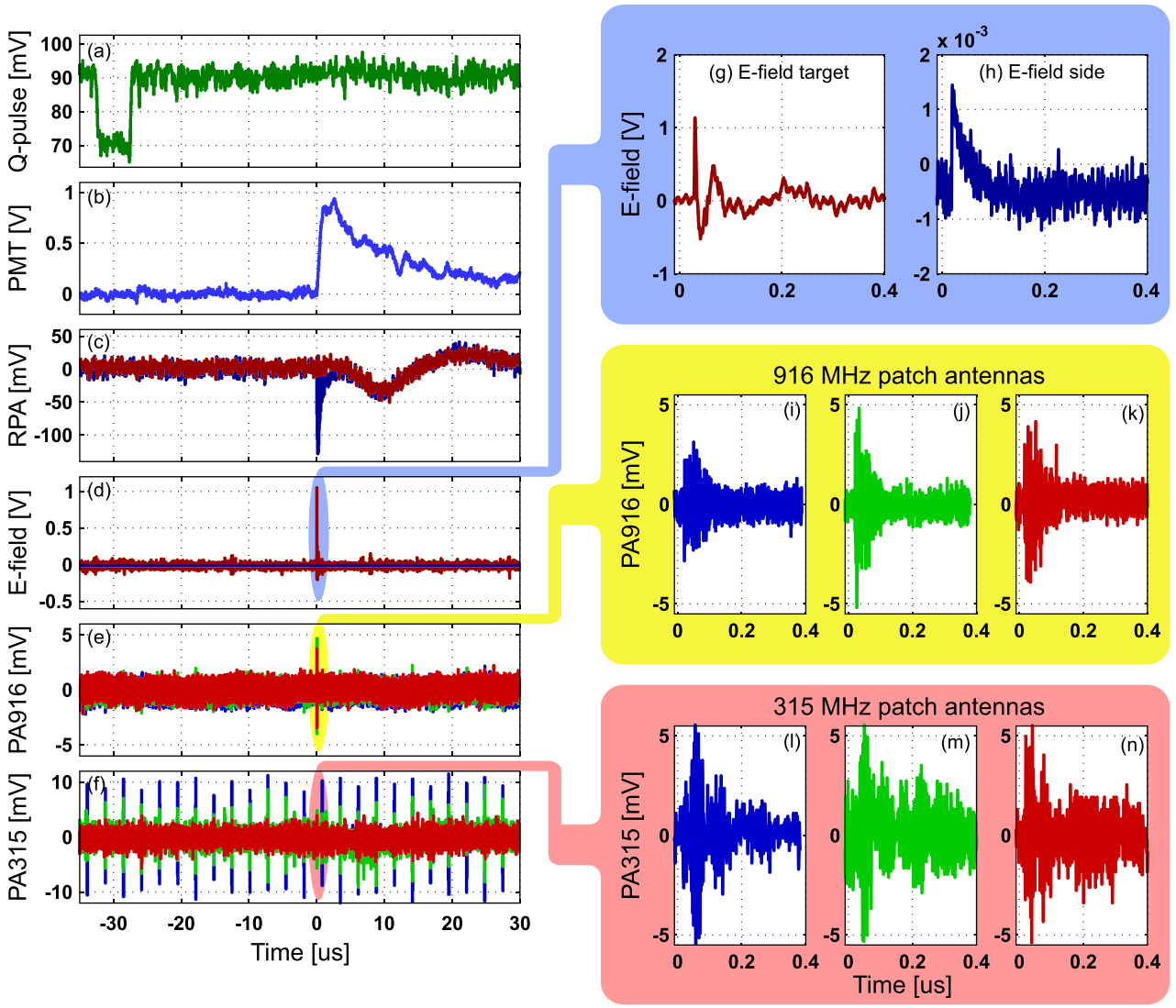

FIG. 3. Multi-sensor response to a hypervelocity micro particle impact. These data shown without post-processing include simultaneous measurements from the full sensor suite generated from the impact of a 1.4×10^{-15} g iron particle traveling at 40 km/s on the E-field target with the target grid biased to 1000 V. These are from top to bottom: (a) the facility's particle sensor or *Q*-pulse (whose pulse width and amplitude scale with speed and charge of the single particle associated with the impact), (b) the PMT, (c) the 2 RPAs, (d) E-field sensors (target and side), (e) the 916 MHz patch antennas, and (f) the 315 MHz patch antennas. The three colored panels to the right are sub-microsecond traces of their respective sensors zoomed in to the time of impact. The top, blue panel contains the two E-field sensors ((g) and (h)), while the middle, yellow panel has the three 916 MHz patch antennas ((i)-(k)), and the bottom, pink panel has the three 315 MHz patch antennas ((l)-(n)).

a space weather event.[14] Data acquisition was managed using three oscilloscopes with sample rates between 1 and 5 GSample/s. Impact confirmation, as well as characterization of the micro particles, resulted from analysis of the facility's particle sensor. The optical flash in the PMT served as a temporal fiducial for impact, where the moment of impact was calibrated using coincidence with response from the E-field sensor. Within nanoseconds of the impact, the patch antennas and the electric field sensors responded. The timing of this RF signal, in addition to the diverse angular placement of the antennas within the chamber with respect to the point of impact, precludes an explanation that the antenna responded from a direct impact by the electrons and instead shows that the RF signal is associated with an emissive mechanism. The patch antenna measured an electric field with magnitude 1.9×10^{-3} V/m at a distance of $\sim$30 cm from the point of impact, while the E-field side sensor detected an electric field with magnitude 1 V/m at a distance of $\sim$1 cm. The patch antennas have a bandwidth that is 10% of their center frequency; note that for the case of a more broadband electromagnetic emission (which we expect from the expanding plasma) the normalization of the amplitudes is best expressed in V m^{-1} Hz$^{-1/2}$. While the timing of the signal in the patch antennas and the location of the patches suggest that an emissive mechanism is responsible for the RF signal, the E-field side sensor is ambiguous and could result from either an emissive mechanism or direct charge transfer. Less than 1 μs later, the electrons arrived at the RPA, producing a large current spike with a peak of 8 nA. The two RPAs were positioned asymmetrically relative to the impact point such that a strong grid or target bias would consistently confine the expanding plasma and its charge constituents into the nearer RPA due to the focusing effect on the plasma. In contrast, signals were detected in both RPAs when targets were grounded due to the larger cone angle of the expanding plasma. A detailed analysis of the RPA measurements is presented by Lee *et al.*[41]

An example spectrogram of the patch antenna data is contained in Fig. 4. These include RF emission data measured simultaneously at 315 MHz and 916 MHz generated by two particles of similar mass and speed separately impacting the active E-field target biased to +1000 V on the grid (left) and the passive tungsten target biased to −1000 V (right). The 315 MHz antennas consistently showed stronger returns than the 916 MHz antennas when RF emission was detected at both frequencies. Note that the data were not normalized for the bandwidth and thus should only be analyzed near the resonant frequency of the antenna.

Inside the impact chamber were high levels of both impulsive and steady-state electromagnetic interference (EMI), as is evidenced by the response in the patch antennas. The ambient EMI environment in the impact chamber complicates the detection of impulsive events. To effectively discriminate impact plasma generated emission from the EMI background, we developed a classification and excision technique for the patch antennas, based on a representation strategy called sparse separation. This technique assumes each data vector can be decomposed into distinct and thus separable morphological components.[42–44] By modeling the patch

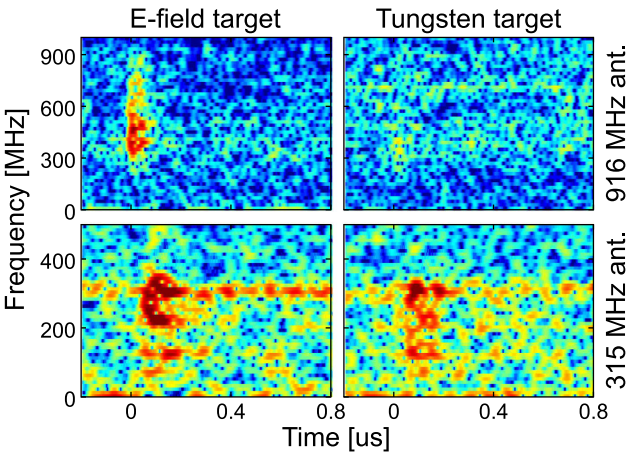

FIG. 4. Spectrograms showing RF emission from a 5×10^{-16} g particle travelling at 50.4 km/s impacting the E-field target biased to +1000 V (left), and from a 9×10^{-16} g particle travelling at 50.7 km/s impacting the passive tungsten target biased to −1000 V (right), generating simultaneous signals in the 315 MHz and 916 MHz antennas. These include the raw data and have not been modified to reflect the bandwidth of the sensor.

antenna measurements as a sparse combination of wavelets and sinusoids, we decompose the signal into periodic signals and oscillatory packets via convex optimization.[45] Separation based on morphological components improves our confidence that the events we have seen are significant and not part of any background noise processes. Fig. 5 shows the two components overlaid on the raw data recorded from one of the 315 MHz patch antennas, for the impact shown in Fig. 1. The repetitive noise as observed here is cleanly separated from the single event coincident with impact. The sparse separation method is capable of both excising periodic components in the EMI, and substantially reducing the level of stochastic EMI. The cleaned RF emission associated with impacts on the gridded tungsten target produced response typically in both the 315 MHz and the 916 MHz patch antennas, while RF emission detected from impacts on the

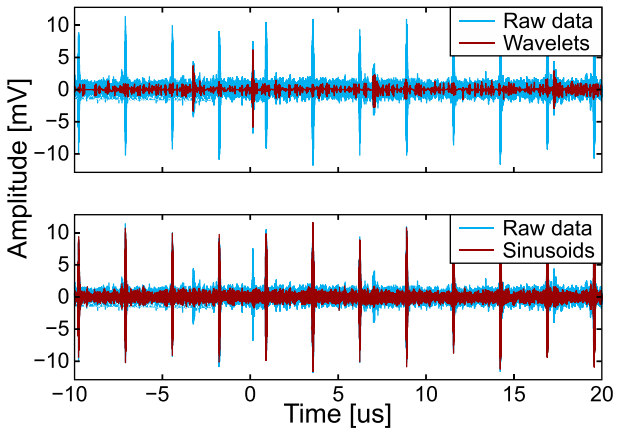

FIG. 5. Time domain representation of the two morphological components (red) separated from the raw 315 MHz patch antenna data (blue). The top panel shows the time domain of the coefficients recovered from the wavelet components of the dictionary. The impulsive spike near 0 μs corresponds to time of impact; two other signals, which are not associated with impact, remain. The bottom panel shows the time domain representation of the coefficients recovered from the Fourier components of the dictionary. The pulsing noise and tones are well supported.

grounded tungsten target produced detectable signals only in the 315 MHz patch antennas.

During the three-week experimental campaign, over 6000 impact events were recorded. These are distributed across three primary experimental parameters: target configuration, target bias, and sensor configuration. Target biases ranging from −1000 V to +1000 V, including grounded, were applied, though experimental constraints limited the number of target-sensor-bias combinations that were tested. There were 2819 during times when the RPAs were installed in the chamber; these are further categorized by target configuration in Table I. Our detection rate (for all 2819 events) for each sensor was the following: PMT (optical) = 64%, RPA (plasma) = 52%, patch antennas (RF) = 1%. However, while RF emission was detected only sporadically from grounded targets, it was routinely detected from high-speed particles impacting highly biased targets. We therefore performed in-depth analysis on the two configurations where RF emission was routinely detected by the patch antennas, including impacts on a +1000 V gridded tungsten target and on a −1000 V bare tungsten target; these total 200 impacts. These 200 impact events are analyzed more fully in Secs. IV–V.

IV. RESULTS

Fig. 6 shows the detection rate for the 200 impact events shaded as a function of the charge produced by impacts derived from the relation $mv^{3.48}$ used by McBride and McDonnell.[31] We found that plasma (i.e., RPA response) is detected for impact speeds greater than ∼8 km/s and RF emission is detected for impact speeds greater than ∼14 km/s. A decreased plasma detection rate is expected for slow impacts, based on the strong dependence of charge production on impact speed. However, the mismatch in speed between when plasma is generated (RPA response) and when RF is generated by the plasma is indicative of a more complex phenomenon than just RF power dependence on charge production. To illustrate the experimental distribution of RF production with particle speed, we examine the detection rate as a function of impact speed. The RF detection rates plotted in Fig. 6 as a function of impact speed are computed as the fraction of impact events that have an associated RF detection within a sliding window. The width of the window spans a factor of four and the calculated rate is plotted at the geometric average of the window limits. These data are shown in Fig. 7, which reveals an increasing trend in detection rate between impact speeds of 10 and 70 km/s; the amplitude of the measured RF signal does not appear to show a dependence on impact speed. The detection rate plotted at an impact speed of 20 km/s considers all impact events between 10 and 40 km/s. A narrower window was not effective because of the sparsity of data available for each specific experimental configuration. The 95% confidence interval around the detection rate, plotted as the shaded region, is approximated as $1.95(p(1-p)/n)^{1/2}$,

TABLE I. Breakdown of the number of impact events by target configuration including material and bias. RF data were recorded properly for 33 of the 35 impacts on bare tungsten at −1000 V and 167 of the 176 impacts on gridded tungsten. These comprise the 200 impacts discussed in Sec. IV. The other 11 impacts in these two configurations did not successfully record the RF signal at the time of impact.

	Targets										
	Bare tungsten	Bare aluminum	Solar panel	Conductive solar cell	Uncoated solar cell	Standard optical solar reflector	Conductive optical solar reflector	Tungsten (E-field 1)	Gridded tungsten (E-field 1)	Copper (E-field 2)	Total
−1000 V	35	24							21	40	120
−500 V	64										64
−300 V	1		148	72	52	43	147				463
−100 V	3				155						158
−75 V					17						17
−50 V	7				11						18
−40 V					18						18
−30 V					77						77
GND	288	19						37	104	41	489
+0 V[a]	20										20
+5 V	41										41
+10 V	83									133	216
+20 V	19										19
+30 V	30										30
+40 V	46										46
+50 V	22										22
+100 V	16				64	102				48	230
+500 V	38										38
+1000 V	102	19						306	176	122	725
FLOAT								8			8
Total	815	62	148	72	394	145	147	351	301	384	2819

[a]+0 V refers to a configuration where the target bias supply voltage is set to zero, rather than directly shorting the target to the vacuum chamber.

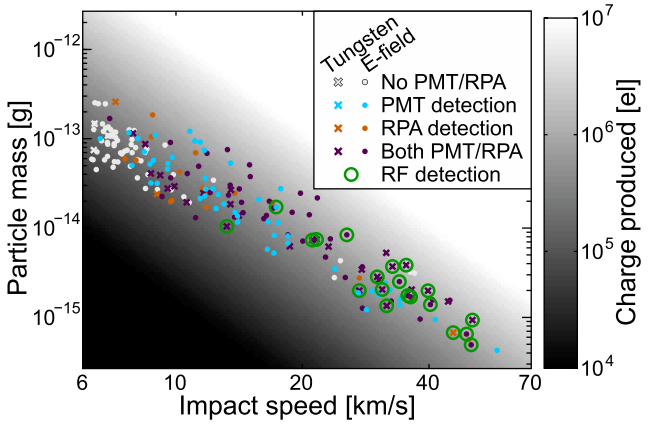

FIG. 6. Particle mass and velocity with charge production. Impacts occurred on gridded (+1000 V) and bare (−1000 V) tungsten targets. The 200 impacts are plotted as a function of particle mass and velocity with impacts on the bare tungsten target indicated by crosses and impacts on the gridded tungsten target indicated by dots. The color of the marker indicates detection by the plasma and optical sensors; grey indicates no detection, blue indicates detection by the PMT, orange indicates detection by at least one RPA, and purple indicates detection by both PMT and RPA. Markers circled in green had an associated RF emission. The expected impact plasma charge produced is plotted as the shaded background in number of electrons. Because of the nature of the accelerator, the slower particles are also the more massive ones and produce 2-3 orders of magnitude less charge than the fastest particles.

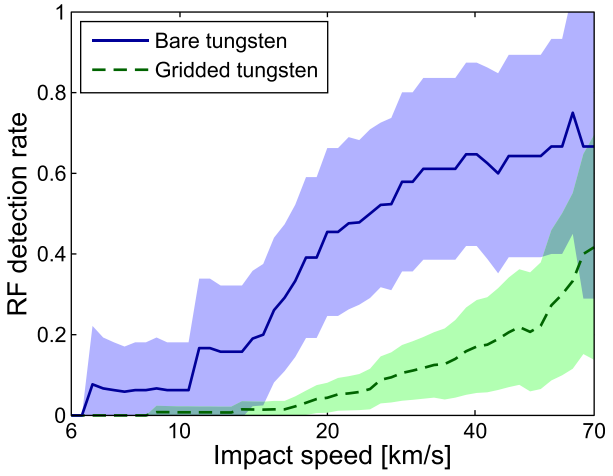

FIG. 7. RF detection rate as a function of impact speed for impacts occurring on gridded (+1000 V) and bare (−1000 V) tungsten targets. Rates were calculated using a moving average with a window of a factor of 4 around the impact speed. The shaded region associated with each trace indicates the 95% confidence interval around the detection rate.

based on the assumption of a Bernoulli process where p is the calculated detection rate within a window and n is the number of events in the window.

V. INTERPRETATION

With the advent of the success of the cell phone industry, a strong motive has emerged to develop RF antennas that are small with respect to the wavelength. Consequently, the technology has moved in the direction of the patch antenna, which is a magnetically tuned circuit, much akin to a classical inductor-capacitor "tank circuit" (used in the description of electronic oscillators used when they were building radios with tubes). At RF frequencies, the inductor and capacitor in the tuned circuit are composed of planar circuit elements that are chosen to resonate at the frequency of interest. Consequently, they have a bandwidth that is relatively narrow compared to the RF frequency, but their resonant character is especially effective at coupling to the electromagnetic field of propagating RF waves in their vicinity. This coupling is especially strong at the resonant frequency and in traditional terms where the size of the aperture relative to the wavelength represents efficiency, it is found that with patch antennas this efficiency approaches unity.[46]

Analyses of both the RPA and patch antenna response allow us to diagnose the mechanism for RF emission. The RPAs measured electron current pulses from both the positively biased gridded target and the negatively biased bare target, and measured positive ions from impacts on targets that were positively biased. Additionally, grounded targets produced RPA measurements that were consistent with our model of electrons arriving first, due to their higher thermal velocities, followed by an ion front. These measurements confirm plasma generation and show that the EM phenomenon detected in the patch antennas is a result of the impact plasma, not simply a discharge of the target material. Further corroboration of EM radiation comes from the nature of the patch antennas. For these antennas, their aperture efficiency is approximately that of an aperture the size of the wavelength of the antenna's center frequency, even though the size of the patch is substantially smaller than the wavelength. The patch achieves this performance via a resonant spatial structure optimized to absorb propagating electromagnetic waves, not static electric fields. However, we must also examine the location with respect to near-field and far-field propagation. The transition between these two regions is commonly understood to be $2D^2/\lambda$, where D is the characteristic scale of the source and λ is the wavelength of the radiation. As D approaches zero, the source becomes an infinitesimal dipole and the EM waves become classical Huygens wavelets. In the case of impact plasma, we have one Huygens source where the wave fronts are expanding spherical surfaces. Our source could potentially produce purely electrostatic or magnetostatic waves, or electromagnetic waves. These waves will all flow outward from the target on spherical wave fronts and illuminate the patch antennas; however, the response of the patch antenna will be weak if the wave is electrostatic. If, however, the patches' structures are illuminated by an EM wave at or near the design frequency, their output will have captured the EM wave's energy over an equivalent aperture the size of the EM's wavelength. From the magnitude of the response we observed, it is reasonable to conclude that the patch antennas responded to illuminating EM waves. Future experiments will continue to focus on this aspect of impact plasma emission.

Previous experimental work has detected RF emission from hypervelocity impacts, but from macroscopic particles greater than 0.1 g traveling at speeds <10 km/s,[20–23] which are ten to 15 orders of magnitude more massive and about a factor of 3 slower than the particles used herein. The

resulting RF emission from these massive particles was instead attributed to microcracking in the target on the scale of 1 μm and with no plasma production.[47] This hypothesis is not relevant or possible for our experiments, where the particle masses are insufficient to produce structural breakdown[48] on the spatial scale attributed to microcracking. Analysis of our target material using an electron microscope with better than 1 μm resolution showed no obvious cratering within the material. Additionally, the RF emission in these previous measurements were detected in a collisional environment with ambient pressures of $\sim$10 Pa; at such pressure plasma charge motion is disrupted by collisions with neutrals in the residual atmosphere. A more physically reasonable explanation of the EMPs we observed is that the RF emission is a direct result of charge motion in the expanding plasma that was detected using our multi-sensor suite. RF emission is not detected with every confirmed impact, which also supports an instability-driven process within the plasma.

VI. CONCLUSIONS

We have detected EMPs associated with micro particle impacts on biased spacecraft surfaces. Based on meteoroid flux models and measurements,[49] a 10^{-9} g meteoroid will impact a 1 m^2 spacecraft approximately once every day in near-Earth space, potentially producing an EMP with each impact under the appropriate speed and bias conditions; note that the sporadic (not shower) meteoroid population dominates at these sizes. We have shown that fast micro particles (>20 km/s) impacting biased surfaces pose the greatest threat to spacecraft because the rate of EMP emission is much higher. Future work includes investigating the pathway through which these electromagnetic fields can cause spacecraft anomalies, as well as analysis of the grounded targets. We recommend that future spacecraft survivability and design studies consider this mechanism.

ACKNOWLEDGMENTS

The authors acknowledge the contributions of Stan Green and Patrick Colestock at LANL, and Rich Adamo at SRI International. Sample target materials were generously donated by J. Likar of Lockheed Martin. Los Alamos National Laboratory funded research conducted in support of this study.

[1]National Research Council, *Limiting Future Collision Risk to Spacecraft: An Assessment of NASA's Meteoroid and Orbital Debris Programs* (National Academies Press, 2011), p. 73.
[2]S. Close, P. Brown, M. Campbell-Brown, M. Oppenheim, and P. Colestock, Icarus **186**, 547 (2007).
[3]P. Brown, R. E. Spalding, D. O. ReVelle, E. Tagliaferri, and S. P. Worden, Nature **420**, 294 (2002).
[4]R. D. Caswell, N. McBride, and A. Taylor, Int. J. Impact Eng. **17**, 139 (1995).
[5]M. J. Neish, M. Takahashi, H. Maejima, H. Kusawake, S. Kawakita, and T. Goka, in *Proceedings of 4th European Conference on Space Debris* (2005), No. 587, p. 705.
[6]P. Jenniskens, Astron. Astrophys. **287**, 990 (1994).
[7]S. Close and S. M. Hunt, Radio Sci. **35**, 1233, doi:10.1029/1999RS002277 (2000).
[8]S. Close, S. M. Hunt, and F. M. McKeen, Radio Sci. **37**, 9-1–9-9, doi:10.1029/2000RS002602 (2002).
[9]J. T. Fentzke and D. Janches, J. Geophys. Res. **113**, A03304, doi:10.1029/2007JA012531 (2008).
[10]N. Meyer-Vernet, M. Maksimovic, A. Czechowski, I. Mann, I. Zouganelis, K. Goetz, M. L. Kaiser, O. C. St. Cyr, J.-L. Bougeret, and S. D. Bale, Sol. Phys. **256**, 463 (2009).
[11]N. Meyer-Vernet, A. Lecacheux, M. L. Kaiser, and D. A. Gurnett, Geophys. Res. Lett. **36**, L03103, doi:10.1029/2008GL036752 (2009).
[12]O. C. St. Cyr, M. L. Kaiser, N. Meyer-Vernet, R. A. Howard, R. A. Harrison, S. D. Bale, W. T. Thompson, K. Goetz, M. Maksimovic, J.-L. Bougeret, D. Wang, and S. Crothers, Sol. Phys. **256**, 475 (2009).
[13]D. A. Gurnett, W. S. Kurth, K. L. Kirchner, G. B. Hospodarsky, T. F. Averkamp, P. Zarka, A. Lecacheux, R. Manning, A. Roux, P. Canu, N. Cornilleau-Wehrlin, P. Galopeau, A. Meyer, R. Boström, G. Gustafsson, J.-E. Wahlund, L. Åhlen, H. O. Rucker, H. P. Ladreiter, W. Macher, L. J. C. Woolliscroft, H. Alleyne, M. L. Kaiser, M. D. Desch, W. M. Farrell, C. C. Harvey, P. Louarn, P. J. Kellogg, K. Goetz, and A. Pedersen, Space Sci. Rev. **114**, 395 (2004).
[14]Z. Wang, D. A. Gurnett, T. F. Averkamp, A. M. Persoon, and W. S. Kurth, Planet. Space Sci. **54**, 957 (2006).
[15]J. W. Warwick, J. B. Pearce, D. R. Evans, T. D. Carr, J. J. Schauble, J. K. Alexander, M. L. Kaiser, M. D. Desch, M. Pedersen, A. Lecacheux, G. Daigne, A. Boischot, and C. H. Barrow, Science **212**, 239 (1981).
[16]J. W. Warwick, D. R. Evans, J. H. Romig, J. K. Alexander, M. D. Desch, M. L. Kaiser, M. Aubier, Y. Leblanc, A. Lecacheux, and B. M. Pedersen, Science **215**, 582 (1982).
[17]M. G. Aubier, N. Meyer-Vernet, and B. M. Pederson, Geophys. Res. Lett. **10**, 5, doi:10.1029/GL010i001p00005 (1983).
[18]D. A. Crawford and P. H. Schultz, Int. J. Impact Eng. **14**, 205 (1993).
[19]D. Crawford and P. Schultz, Int. J. Impact Eng. **23**, 169 (1999).
[20]T. Takano, Y. Murotani, K. Maki, T. Toda, A. Fujiwara, S. Hasegawa, A. Yamori, and H. Yano, J. Appl. Phys. **92**, 5550 (2002).
[21]K. Maki, T. Takano, A. Fujiwara, and A. Yamori, Adv. Space Res. **34**, 1085 (2004).
[22]K. Maki, E. Soma, T. Takano, A. Fujiwara, and A. Yamori, J. Appl. Phys. **97**, 104911 (2005).
[23]H. Ohnishi, K. Maki, E. Soma, S. Chiba, T. Takano, and A. Yamori, in *Proceedings of the URSI-GA*, Delhi (2005).
[24]R. Bianchi, F. Capaccioni, P. Cerroni, M. Coradini, E. Flamini, P. Hurren, G. Martelli, and P. N. Smith, Nature **308**, 830 (1984).
[25]G. Martelli and P. Cerroni, Phys. Earth Planet. Inter. **40**, 316 (1985).
[26]S. G. O'Keefe and D. V. Thiel, Phys. Earth Planet. Inter. **89**, 127 (1995).
[27]L. Foschini, Europhys. Lett. **43**, 226 (1998).
[28]D. E. Austin, R. L. Grimm, H. L. K. Manning, C. L. Bailey, J. E. Farnsworth, T. J. Ahrens, and J. L. Beauchamp, J. Geophys. Res. **108**, 5038, doi:10.1029/2002JE001947 (2003).
[29]S. Close, P. Colestock, L. Cox, M. Kelley, and N. Lee, J. Geophys. Res. **115**, A12328, doi:10.1029/2010JA015921 (2010).
[30]P. R. Ratcliff, M. J. Burchell, M. J. Cole, T. W. Murphy, and F. Allahdadi, Int. J. Impact Eng. **20**, 663 (1997).
[31]N. McBride and J. A. M. McDonnell, Planet. Space Sci. **47**, 1005 (1999).
[32]H. Dietzel, G. Neukum, and P. Rauser, J. Geophys. Res. **77**, 1375, doi:10.1029/JB077i008p01375 (1972).
[33]J. A. M. McDonnell, S. P. Deshpande, D. H. Niblett, M. J. Neish, and P. J. Newman, Adv. Space Res. **13**, 87 (1993).
[34]V. C. Frost, Meteoroid Damage Assessment, Technical Report SP-8042, NASA, 1970.
[35]N. Lee, S. Close, D. Lauben, I. Linscott, A. Goel, T. Johnson, J. Yee, A. Fletcher, R. Srama, S. Bugiel, A. Mocker, P. Colestock, and S. Green, Int. J. Impact Eng. **44**, 40 (2012).
[36]Z. Ceplecha, J. Í. Borovička, W. G. Elford, D. O. ReVelle, R. L. Hawkes, V. Í. Porubčan, and M. Šimek, Space Sci. Rev. **84**, 327 (1998).
[37]A. Mocker, S. Bugiel, S. Auer, G. Baust, A. Colette, K. Drake, K. Fiege, E. Grün, F. Heckmann, S. Helfert, J. Hiller, S. Kempf, G. Matt, T. Mellert, T. Munsat, K. Otto, K. Postberg, H.-P. Röser, A. Shu, Z. Sternovsky, and R. Srama, Rev. Sci. Instrum. **82**, 095111 (2011).
[38]R. Evans, H. Garrett, S. Gabriel, and A. Whittlesey, in *Proceedings of the Spacecraft Charging Technology Conference* (1989), Vol. 2, p. 615
[39]J. F. Friichtinicht and J. C. Slattery, Ionization associated with hypervelocity impact, NASA Technical Note TN-D-2091, 1963.
[40]S. Auer, E. Grün, P. Rauser, V. Rudolph, and K. Sitte, Space Res. **8**, 606 (1968).
[41]N. Lee, S. Close, A. Goel, D. Lauben, I. Linscott, T. Johnson, D. Strauss, S. Bugiel, A. Mocker, and R. Srama, Phys. Plasmas **20**, 032901 (2013).

[42]M. J. Fadili, J.-L. Starck, J. Bobin, and Y. Moudden, Proc. IEEE **98**, 983 (2010).
[43]J.-L. Starck, M. Elad, and D. L. Donoho, IEEE Trans. Image Process. **14**, 1570 (2005).
[44]A. M. Bruckstein, D. L. Donoho, and M. Elad, SIAM Rev. **51**, 34 (2009).
[45]D. Chang, SIAM J. Imaging Sci. **2**, 183 (2009).
[46]K. R. Carver and J. Mink, IEEE Trans. Ant. Propagation **29**, 2–24 (1981).
[47]H. Ohnishi, S. Chiba, E. Soma, K. Ishii, K. Maki, T. Takano, and S. Hasegawa, J. Appl. Phys. **101**, 124901 (2007).
[48]S. Drapatz and K. W. Michel, Z. Naturforsch. Teil A **29**, 870 (1974).
[49]E. Grün, H. A. Zook, H. Fechtig, and R. H. Giese, Icarus **62**, 244 (1985).